Grid integration of a 500 kW alkaline electrolyzer system for harmonic analysis and robust control

Zhao, Weihao; Nielsen, Morten Rahr; Kjær, Martin; Iov, Florin; Munk-Nielsen, Stig

Published in:
e-Prime: Advances in Electrical Engineering, Electronics and Energy

DOI (link to publication from Publisher):
10.1016/j.prime.2023.100217

Publication date:
2023

Document Version
Publisher's PDF, also known as Version of record

e-Prime - Advances in Electrical Engineering, Electronics and Energy 5 (2023) 100217

Contents lists available at ScienceDirect

e-Prime - Advances in Electrical Engineering, Electronics and Energy

journal homepage: www.elsevier.com/locate/prime

Grid integration of a 500 kW alkaline electrolyzer system for harmonic analysis and robust control

Weihao Zhao *, Morten Rahr Nielsen, Martin Kjær, Florin Iov, Stig Munk Nielsen

AAU Energy, Aalborg University, Aalborg 9220, Denmark

ARTICLE INFO

Keywords:
Power-to-X
Green hydrogen
Alkaline electrolyzer
Harmonic analysis
Medium voltage converter

ABSTRACT

In the past decades, wind and solar energy installation has rapidly increased. The electric grid has been ever increasingly penetrated with such intermittent renewable sources, which inevitably increase the schedule difficulty and cause stability issues. To solve such problems and efficiently utilize the renewable energy, electrolyzer plants are integrated into the grid. This work provides a simulation result of a 500 kW alkaline electrolyzer system including converter topology and electrolyzer performance modeling. Two case studies are carried out in MATLAB®/Simulink® and PLECS to investigate the harmonic distortion and system response during voltage deviation in the distribution grid. The simulation result indicates that different short circuit ratio values affect the total harmonic distortion and the harmonic sidebands are mainly affected by controller bandwidth and switching frequency. The designed system maintains 95% DC link voltage even when subjected to a 20% voltage dip in the point of connection.

1. Introduction

In the past decades, a rapid increase in renewable energy production happened around the world. From 2000 to 2021, the worldwide wind energy capacity increased from 2.24% to 26.83% of the total renewable energy capacity. In the same period, worldwide solar energy capacity increased from 0.16% to 27.85% of the total renewable energy capacity [1]. These two renewable energy sectors are the main contributors to renewable electricity production and green energy transition. The rapid growth of wind and solar sectors is partly driven by technology advancement and policy stimulus. With these supports, the total Levelized Cost of renewable Electricity (LCoE) has dropped significantly, which makes renewable electricity prices cheaper than conventional electricity prices. Nowadays, Denmark is establishing two gigawatt-scale energy islands (wind power hubs), which will connect neighboring countries and provide renewable electricity to local citizens [2]. This project is expected to leverage the energy shortage problems and contribute to the 100% renewable energy ambition. As wind and solar sectors are intermittent and highly dependent on weather conditions, the ever-increasing penetration of them makes the scheduling of power systems more risky and unpredictable. In some cases, surplus renewable energy has to be curtailed in order to secure a stable operation of the grid [3].

To solve this problem and make efficient utilization of renewable energy, Power-to-X (PtX) concept is proposed by researchers and driven by industry partners. According to the Danish Energy Agency [4], PtX is a blanket term for a number of technologies that are all based on using electricity to produce hydrogen. The produced hydrogen can subsequently be used directly as a fuel for road transport and industrial purposes, or further converted into other fuels, chemicals, and materials. Based on the method used to produce hydrogen, it is classified into four categories:

- **Grey hydrogen:** produced from natural gas through the process of steam reforming, which emits a large amount of CO_2 when burning natural gas.
- **Brown hydrogen:** produced from coal or lignite through the process of gasification, which emits a large amount of CO_2 when burning coal or lignite.
- **Blue hydrogen:** produced from fossil fuels, in which most of the CO_2 emission can be captured and deposited underground.
- **Green hydrogen:** produced from high purity water through the process of water electrolysis, which is a CO_2 neutral process. The electricity used in the process comes from renewable sources.

In the aforementioned energy islands, green hydrogen production will be used as one of the technologies to efficiently utilize renewable

* Corresponding author.
E-mail address: wzh@energy.aau.dk (W. Zhao).

https://doi.org/10.1016/j.prime.2023.100217
Received 28 November 2022; Received in revised form 23 June 2023; Accepted 18 July 2023
Available online 26 July 2023

Nomenclature

Acronyms

AC	alternating current
DC	direct current
ALK	alkaline electrolyzer
PEM	proton exchange membrane electrolyzer
SOE	solid oxide electrolyzer
AEM	anoin exchange membrane
CAPEX	capital expenditure
AFE	active front end
PSFB	phase shifted full-bridge
THD	total harmonic distortion
PoC	point of connection
RMS	root mean square
SCR	short circuit ratio

Symbols

$N_p : N_s$	transformer turns ratio
C_f	filter capacitor, μF
R_d	damping resistor, Ω
V_{dc}	DC-link voltage, kV
f_{line}	line frequency, Hz
f_{sw}	switching frequency, Hz
f_{res}	resonant frequency, Hz
ω	angular frequency, rad/s
e_{abc}	grid side voltage, kV
i_{abc}	grid side current, A
P_{rated}	rated power, kW
e_{dq}	*d*-axis and *q*-axis voltage, kV
Δi_{dq}	*d*-axis and *q*-axis current change, A
K_p	proportional gain
T_s	time delay, s
Z_b	base impedance, Ω
L_b	base inductance, mH
G_0	DC gain
V_{load}	load voltage, V
G_{pv}	voltage loop transfer function
G_{op}	open-loop transfer function
R_c	ESR of the inductor, Ω
V_{ely}	electrolyzer voltage, V
V_{rev}	reversible voltage, V
V_{act}	activation voltage, V
V_{ohm}	ohmic voltage, V
ΔG	change in Gibbs energy, J mol^{-1}
ΔH	change in enthalpy, J mol^{-1}
ΔS	change in entropy, J mol^{-1}
T	temperature, °C
V_{th}	thermoneutral voltage, V
z	number of electrons transferred per reaction
N_s	number of cells in series
$r_{1,2}$	coefficient for ohmic resistance, Ω m^2
s	coefficient for overvoltage on electrode,V
t	coefficient for overvoltage on electrode, A m^2
η_F	Faraday efficiency
R_{ohm}	ohmic resistance of electrolyzer cell, Ω
η_e	energy efficiency
$f_{1,2}$	parameters related to the Faraday efficiency
A	area of the electrode, m^2
P	pressure, bar
$\dot{n}_{H_2}$	hydrogen flow rate, Nm^3/h
$\dot{n}_{O_2}$	oxygen flow rate, Nm^3/h
I_{ely}	electrolyzer current, A
L_g	grid-side inductor, mH
L_c	converter-side inductor, mH
K_r	ripple factor
i_{dq}	*d*-axis and *q*-axis current, A
$\Delta I_{\max}$	maximum current change, A
I_{load}	load current, A
$I_{\max}$	maximum current, A
C_b	base capacitance, μF
T_i	integral time constant, s

Constants

F	Faraday's constant, 96,485 C mol^{-1}
R	universal gas constant, 8.315 J K^{-1} mol^{-1}
v_{std}	volume of ideal gas 0.0224136 m^3 mol^{-1}

energy. The conceptual visualization of renewable energy generation coupled with green hydrogen production is presented in Fig. 1. Electricity generated from solar panels and wind turbines is transmitted by transmission networks and distributed to end users. During periods of surplus generation, renewable electricity is used to produce hydrogen which is transported via a pipeline or stored in a storage facility. During periods of deficit generation, electrolyzer plants can reduce the operation power or even regenerate power (i.e., solid oxide electrolyzer in fuel cell mode) to support grid frequency and voltage stability.

Nowadays, three main electrolyzer technologies are used in the commercial or early-commercial stage. Meanwhile, one technology is still in the laboratory stage. Namely, they are: (a) Alkaline (ALK) electrolyzer, (b) Proton Exchange Membrane (PEM) electrolyzer, (c) Solid Oxide Electrolyzer (SOE), (d) Anion Exchange Membrane (AEM) electrolyzer. ALK electrolyzers have been used in industry for nearly a century, however, PEM electrolyzers are recently commercialized. SOE is a new technology in the early-commercial stage. From existing commercial products, the efficiency of SOE is around 3.3 ∼ 3.6 kWh/Nm^3, which is the highest efficiency record among other electrolyzer technologies [5]. However, the lifetime of SOE is far less than the lifetime of ALK and PEM electrolyzers due to immature technologies and harsh operation conditions (i.e., 750 °C temperature [6]). At the moment when this study is prepared, ALK and PEM electrolyzers dominate the global market. Based on commercially available products, a comparison between ALK and PEM technologies is presented in Table 1.

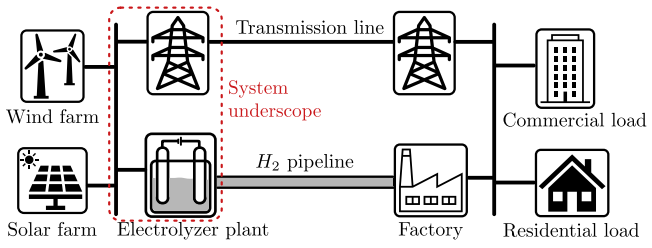

Fig. 1. Electricity-hydrogen combined power system for efficient renewable energy utilization..

The ALK electrolyzers are commercially predominant due to their technical maturity and economic advantages (i.e., lower Capital Expenditure (CAPEX) and higher efficiency). The study carried out in this article is based on ALK electrolyzers, but the methodology presented is applicable to other types of electrolyzer systems, i.e., PEM and SOE, with proper adaptations.

The current solution for commercial electrolyzer power supply is thyristor and diode based topologies [10–12]. They have a low degree of

Table 1
Comparison between ALK and PEM electrolyzers (CAPEX stands for capital expenditure) [7–9].

Specification	ALK	PEM	Units
Efficiency	4.82	5.8	[kW h/Nm^3]
Cell Pressure	1 ∼ 30	30 ∼ 60	[bar]
Efficiency[a]	65 ∼ 68	57 ∼ 64	[%]
Lifetime Stack	8 ∼ 10	4 ∼ 5	[× 10^4 h]
CAPEX[b]	480 ∼ 750	700 ∼ 1200	[€ /kW]
Load range	15 ∼ 100	0 ∼ 160	[%]
Ramp rate	0.2 ∼ 25	100	[%/s]

[a] LHV: Lower Heating Value (H_2: 120 MJ kg^{-1}).
[b] CAPEX: Total Capital Expenditure including power supply and installation cost.

controllability, high current ripples at the load side, slow dynamic response, and high harmonic distortion. There is a trend to shift from the passive or semi-controlled power device to fully controlled power devices. In this study, the active front end (AFE) and phase shifted full bridge (PSFB) converter is proposed as an alternative solution for the electrolyzer power supply. A comparison between this work and state-of-the-art literature is presented in Table 2. It mainly considers two aspects: (a) electrolyzer model, and (b) grid compliance. An accurate electrolyzer model can reflect the system dynamics, and therefore, lead to an accurate and stable controller and filter design. Meanwhile, most of the electrolyzer plants connect to the electrical grid. Hence, they need to comply with the grid code to secure the power system stability. Since the previous literature on the modeling of electrolyzer converters neglect the system non-linearity and dynamics [13–19], it results in an inaccurate model, and cannot be used for the controller design.

In this paper, the electrolyzer is modeled with electrochemical equations considering the non-linearity and dynamics. The main objective of this study is (a) investigation of the grid code compliance with the proposed converter topology, (b) co-simulation with electrolyzer and electrical converter considering the non-linearity, (c) tuning the power converter controller and LCL filter considering the non-linearity of electrolyzer stacks.

2. Modeling of alkaline electrolyzer

Over the last decade, a number of modeling studies for ALK electrolyzers have been presented in the literature. Most of the modeling methods proceed from basic equations and apply to a specific electrolyzer cell. The final models are varied according to authors' backgrounds and applications. They start from simple linear models that only describe the steady-state operation of cells [23,24] to more detailed multi-physics models that capture the temperature and pressure dependency and thermodynamics [25–27].

An alkaline electrolysis cell has two electrodes which are physically separated by a diaphragm and immersed in a liquid electrolyte as shown in Fig. 2. The electrolyte is generally 25–30% KOH base. The corresponding chemical reactions that happened at the anode and cathode

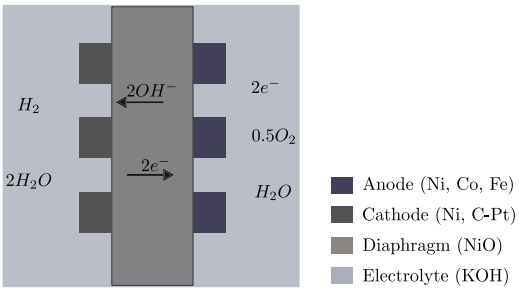

Fig. 2. Schematic plot of alkaline water electrolysis cell with chemical reaction [28].

are given:

$$\begin{aligned} \text{Anode}: &\quad 2OH^- \rightarrow 0.5O_2 + H_2O + 2e^- \\ \text{Cathode}: &\quad 2H_2O + 2e^- \rightarrow H_2 + 2OH^- \end{aligned} \tag{1}$$

For a full-scale system-level study including power converters, the linear model is too simple to capture enough information about electrolyzer cells, and the multi-physics model is too complicated to be computationally efficient. In the following section, the empirical equation method is selected to model the ALK electrolyzers, which has a good compromise between computation cost and accuracy.

2.1. Empirical equations model

The electrolyzer cell voltage, V_{ely}, is commonly modeled as (2) in literature [23–28].

$$V_{ely} = V_{rev} + V_{act} + V_{ohm} \tag{2}$$

where V_{ely} is the electrolyzer voltage, V_{rev} is the reversible voltage, V_{ohm} is the ohmic voltage drop across the electrolyzers, and V_{act} is the activation voltage caused by activation phenomena at electrodes.

2.1.1. Reversible voltage

The reversible voltage, V_{rev}, is defined as the electromotive force for a reversible electrochemical process. Ulleberg [26] uses the Gibbs free energy to estimate the reversible voltage, as shown in (3).

$$V_{rev} = \frac{\Delta G}{zF} \tag{3}$$

where: ΔG is the Gibbs energy with unit [KJ mol^{-1}], which is the difference between the enthalpy ΔH and entropy ΔS of chemical reactions. F is the Faraday's constant and z is the number of electrons transferred per reaction.

$$\Delta G = \Delta H - T\Delta S \tag{4}$$

Ehthalpy is the amount of energy needed to make the chemical reaction happen, and entropy is the amount of energy produced from the

Table 2
Comparison between the state-of-the-art literature and this work.

Ref.	Electrolyzer model	Grid connection	Harmonic analysis	Grid code	Topology	Controller
[15]	RC network + DC source	Yes	No	No	AFE + DAB	PQ
[17]	RC network + DC source	No	No	No	Buck	PI
[16]	Linear approximation	No	No	No	Diode rectifier + PSFB	PI
[13]	No	No	No	No	DC/DC converters	No
[14]	No	No	No	No	Thyristor rectifier	No
[18]	Linear approximation	No	No	No	LLC resonant converter	PI
[20]	RC network + DC source	Yes	No	No	Diode rectifer + Buck converter	PID
[19]	Linear approximation	Yes	No	No	Diode rectifier + PSFB	PI
[21]	RC network + DC source	Yes	Yes	No	Thyristor rectifier	PI
[22]	Electrochemical model	Yes	Yes	No	Thyristor + diode rectifier	PI
This work	Electrochemical model	Yes	Yes	Danish	AFE + PSFB	PI

chemical reaction. The thermoneutral cell voltage, V_{tn}, is expressed by:

$$V_{tn} = N_s \frac{\Delta H}{zF} \tag{5}$$

According to Ulleberg [26], the reversible voltage is temperature and pressure dependent, but the thermoneutral voltage is less temperature and pressure dependent.

2.1.2. Ohmic and activation voltage

In order to properly model the temperature dependence of the electrolyzer, Ulleberg [29] proposed a modified model in (6).

$$\begin{cases} V_{ohm} = N_s \dfrac{R_{ohm}}{A} I_{ely} \\ R_{ohm} = r_1 + r_2 (T - 273.15) \end{cases} \tag{6}$$

Where: V_{ohm} is the ohmic voltage drop. r_1 and r_2 are temperature coefficient.

The over voltage caused by activation effects, V_{act}, are described by Ulleberg [29]:

$$\begin{cases} V_{act} = N_s s log_{10}\left(\dfrac{K_{act}}{A} I_{ely} + 1\right) \\ K_{act} = t_1 + \dfrac{t_2}{(T - 273.15)} + \dfrac{t_3}{(T - 273.15)^2} \end{cases} \tag{7}$$

where: s, t_1, t_2, and t_3 are parameters used to describe the temperature dependency of electrolyzer cells.

There are two efficiencies used to describe the operation of electrolyzers. One is Faraday efficiency (η_F) and another is energy efficiency (η_e). The Faraday efficiency is defined as the ratio between the actual and theoretical maximum amount of hydrogen produced in the electrolyzer [26]. It is calculated as:

$$\eta_F = \frac{(I/A)^2}{f_1 + (I/A)^2} f_2 \tag{8}$$

where f_1 and f_2 are Faraday efficiency related parameters.

Due to the existence of leakage current, the value of Faraday efficiency is below 1. The energy efficiency is calculated by:

$$\eta_e = \frac{V_{tn}}{V_{ely}} \tag{9}$$

The hydrogen production rate of electrolyzers is directly proportional to the number of electrons transferred at electrodes, which is related to the current supplied by external circuits. Hence, the hydrogen production rate, $\dot{n}_{H_2}$ from an electrolyzer is expressed as Ulleberg [26]:

$$\dot{n}_{H_2} = \eta_F \frac{N_s I_{ely}}{zF} \tag{10}$$

According to stoichiometry relation, the oxygen production rate, $\dot{n}_{O_2}$, and water consumption rate $\dot{n}_{H_2O}$ are expressed as:

$$\dot{n}_{H_2O} = \dot{n}_{H_2} = 2\dot{n}_{O_2} \tag{11}$$

The final empirical model of an ALK electrolyzer is presented in Fig. 3.

2.2. Characterization of alkaline electrolyzer

The electrolyzer data is provided by GreenHydrogen.dk, Siemens, DTU, and AU [30]. Based on curve fitting results, the critical parameters are presented in Table 3, and the final polarization curve is given in Fig. 4. Due to the limited data obtained from GreenHydrogen.dk, Siemens, DTU, and AU [30], only the rated condition ($T = 80\,^{\circ}C$ and $P = 20$ bar) is considered in this study. In real applications, temperature and pressure controllers can maintain the temperature and pressure constant as their rated values during normal operation. In Fig. 4, the largest error for the developed model is below 0.25%, which is sufficiently accurate for further studies.

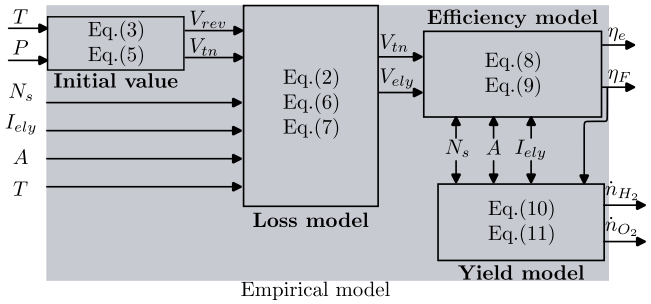

Var.	Description	Var.	Description
P	Pressure [bar]	V_{rev}	Reverse voltage [V]
T	Temperature [K]	V_{tn}	Thermoneutral voltage [V]
I_{ely}	Current [A]	V_{ely}	Electrolyzer voltage [V]
N_s	Cell number [-]	η_F	Faraday efficiency [%]
A	Area [m^2]	η_e	Energy efficiency [%]
$\dot{n}_{O_2}$	O_2 flow rate [Nm^3/h]	$\dot{n}_{H_2}$	H_2 flow rate [Nm^3/h]

Fig. 3. Schematic plot of electrolyzer empirical model including definition of main variables.

Table 3
Critical parameters of the characterized electrolyzer.

Variable	Value	Variable	Value
R_{ohm} [Ω m^2]	3.17	s [V]	0.123
K_{act} [A/m^2]	31.19	N_s [−]	98
A [m^2]	0.3	V_{rev} [V]	1.2532

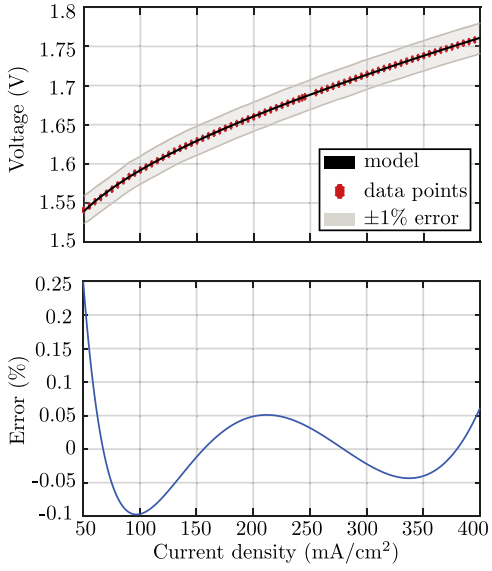

Fig. 4. Accuracy comparison between characterized ALK model and data points provided from GreenHydrogen.dk, Siemens, DTU, and AU [30].

3. Design and modeling of electrolyzer converter

The investigated converter topology in Fig. 5 consists of a 10 kV isolation transformer (Δ/Y connection) with a turns ratio 4:1, an AFE rectifier and PSFB converter. The AFE converter converts the 2.5 kV (rms) AC input to 6 kV DC output and the PSFB converter provides high

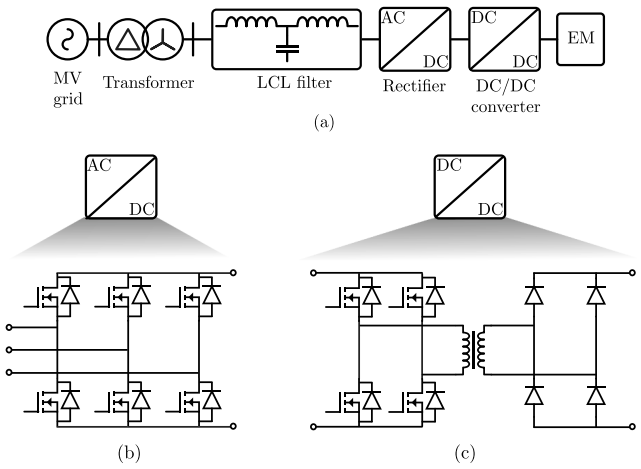

Fig. 5. (a) System structure of a 500 kW electrolyzer system (EM: electrolyzer module), (b) topology of AC/DC rectifier (active-front-end rectifier), (c) topology of DC/DC converter (phase-shifted full-bridge converter).

current output to the electrolyzer stacks. In order to have high performance (i.e., high power factor, low THD, and stable operation), the LCL filter, current loop controller, and voltage loop controller have to be properly designed. In the subsequent section, the design principle of the LCL filter, voltage and current controllers are presented.

3.1. Design of LCL filter

The detailed system structure with LCL filter is presented in Fig. 6. The LCL filter consists of five elements for each phase. Namely, they are grid side inductor (L_g), converter-side inductor (L_c), equivalent series resistance (R_c), filter capacitor (C_f), and damping resistor (R_d). The design process of the LCL filter is presented in Fig. 7 referring [31]. A design example for a 500 kW electrolyzer system is presented below:

- **Step 1:** Input system technical parameters: input power (P_{rated}) of 500 kW, line frequency (f_{line}) of 50 Hz, line to line voltage (V_{rated}) of 10 kV, DC link voltage (V_{dc}) of 6 kV, and switching frequency (f_{sw}) of 4 kHz.
- **Step 2:** Calculate base impedance (Z_b) of 200 Ω, base inductance (L_b) of 637 mH, capacitance (C_b) of 15.92 μF, and maximum current ($I_{\max}$) of 40.825 A.

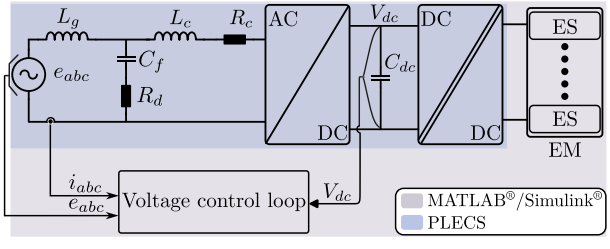

L_c	Converter-side inductor	C_f	Filter capacitor
R_c	ESR of filter inductor	L_g	Grid-side inductor
R_d	Damping resistor	ES	Electrolyzer stack

Fig. 6. Single line diagram with LCL filter and voltage control loop.

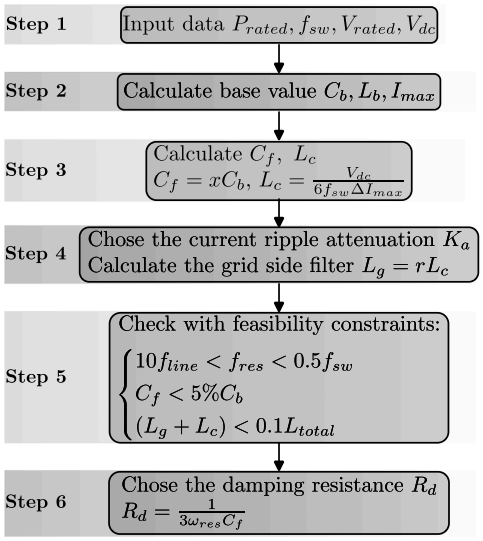

Fig. 7. The LCL filter design process.

$$\begin{cases} Z_b = \dfrac{V_{rated}^2}{P_{rated}} \\ L_b = \dfrac{Z_b}{\omega_{line}} \\ C_b = \dfrac{1}{Z_b\omega_{line}} \\ I_{\max} = \dfrac{\sqrt{2}P_{rated}}{\sqrt{3}V_{rated}} \end{cases} \tag{12}$$

- **Step 3:** By selecting the current ripple factor (K_r) to 0.35 and the capacitance sizing factor (x) to 4%, which should below 5% for not decreasing the power factor at rated power [31], then according to Eq. (13), a maximum current ripple ($\Delta I_{\max}$) of 14.29 A, a converter side inductance (L_c) of 17.5 mH, and a filter capacitance (C_f) of 0.636 μF are obtained.

$$\begin{cases} \Delta I_{\max} = K_r I_{\max} \\ L_c = \dfrac{V_{dc}}{6f_{sw}\Delta I_{\max}} \\ C_f = xC_b \end{cases} \tag{13}$$

- **Step 4:** By choosing the current ripple attenuation level (K_a) of 10%, then according to Eq. (14), the resulting grid side inductance (L_g) of 31.9 mH is obtained.

$$\begin{cases} L_g = rL_c \\ r = \dfrac{1 + \dfrac{1}{K_a}}{L_c C_f \omega_{sw}^2 - 1} \end{cases} \tag{14}$$

- **Step 5:** According to Eq. (15), the resonant frequency (f_{res}) is approximately 1.8 kHz.

$$\begin{cases} f_{res} = \dfrac{1}{2\pi}\sqrt{\dfrac{L_c + L_g}{L_c L_g C_f}} \\ 10f_{line} < f_{res} < 0.5f_{sw} \end{cases} \tag{15}$$

- **Step 6:** According to Eq. (16), the damping resistance (R_d) is 66.6 Ω.

$$R_d = \frac{1}{3\omega_{res} C_f} \tag{16}$$

3.2. Controller design

The controller structure is presented in Figs. 8 and 9. It consists of an outer voltage loop controller and inner current loop controller. The current loop controller regulates the current magnitude flowing through the filter inductor and the current phase angle at the PoC. The voltage loop controls the magnitude of the DC link voltage. For the system in Fig. 6, the design process is given:

- **Step 1:** Sample grid side voltage (e_{abc}) and grid side current (i_{abc}), and transform them from the stationary *abc* reference frame to the rotating *dq* reference frame to obtain e_{dq} and i_{dq}.
- **Step 2:** Based on KVL, the system in *dq* frame is defined with the following equations, where filter capacitance (C_f) is neglected.

$$\begin{cases} e_d = R_c i_d + (L_g + L_c)\dfrac{\mathrm{d}i_d}{\mathrm{d}t} + v_d - \omega(L_g + L_c) i_q \\ e_q = R_c i_q + (L_g + L_c)\dfrac{\mathrm{d}i_q}{\mathrm{d}t} + v_q + \omega(L_g + L_c) i_d \end{cases} \tag{17}$$

- **Step 3:** By moving the coupling term $\pm\omega(L_g + L_c) i_{dq}$ to the left side of the equation, the system transfer function is obtained. Since the transfer function at *d*-axis is the same as transfer function at *q*-axis, the *d*-axis transfer function is taken as an example.

$$\begin{cases} G_{pc} = \dfrac{i_{dq}}{\Delta v_{dq}} = \dfrac{1}{s(L_g + L_c) + R_c} \\ \Delta v_{dq} = e_{dq} - v_{dq} \pm \omega(L_c + L_g) i_{qd} \end{cases} \tag{18}$$

- **Step 4:** Considering a sample and computation delay (T_s) of 250 μs, the PI controller is designed with symmetrical optimum [32], where G_{op} is the open loop transfer function, $T_{\sum}$ is the sum of insignificant time constants, T_1 is the significant time constant, and G_0 is the DC gain.

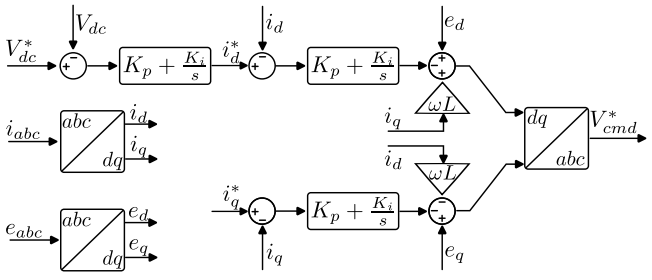

Fig. 8. The system controller realized in the simulation with reference frame transformation.

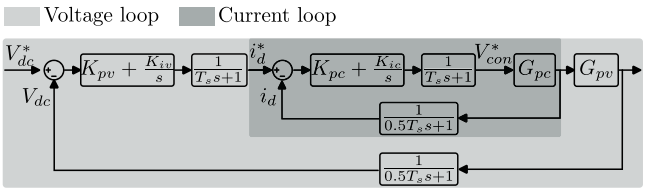

Fig. 9. The control block diagram for current and voltage control loops.

$$\begin{cases} G_{op} = \dfrac{G_0}{\left(sT_{\sum} + 1\right)(sT_1 + 1)} \\ T_{\sum} = 4T_s \\ T_1 = \dfrac{L_c + L_g}{R_c} \\ K_p = \dfrac{T_1}{2G_0 T_{sum}} \\ T_i = 4T_{\sum} \\ G_0 = \dfrac{1}{R_c} \end{cases} \tag{19}$$

- **Step 5:** Referring to Fig. 6 and [33], the transfer function of the voltage plant is obtained with:

$$\begin{cases} G_{pv} = \dfrac{\sqrt{3}}{2}\dfrac{R_{load}}{(1 - R_{load} C_{dc} s)} \\ R_{load} = \dfrac{V_{dc}^2}{P_{rate}} \end{cases} \tag{20}$$

- **Step 6:** By considering the significant time constant (τ_c) introduced by the current control loop, the voltage controller is designed with symmetrical optimum [32].

$$\begin{cases} G_{op} = \dfrac{G_0}{\left(sT_{\sum} + 1\right)(sT_1 + 1)} \\ T_{\sum} = 1.5T_s + \tau_c \\ T_1 = \dfrac{C_{dc}}{R_o} \\ K_p = \dfrac{T_1}{2G_0 T_{\sum}} \\ T_i = 4T_{\sum} \\ G_0 = \dfrac{\sqrt{3} R_{load}}{2} \end{cases} \tag{21}$$

Since the resulting control algorithms are implemented in the *z* domain, the corresponding transfer functions are discretized and compared with the *s* domain in Fig. 10. The limited sampling frequency reduces the system stability margin in the *z* domain transfer function compared with the one in the *s* domain. With the symmetrical optimum design criteria stated in the controller design process, the system stability margin is maintained at a positive value for both the *s* and *z* domains.

The bandwidth of the current loop is 2.249×10^3 rad/s and the voltage loop is 494 rad/s. Both of them are far below the resonance frequency of the LCL filter (1.18×10^4 rad/s). According to [36], the phase lag and gain difference between a LCL filter and L filter is

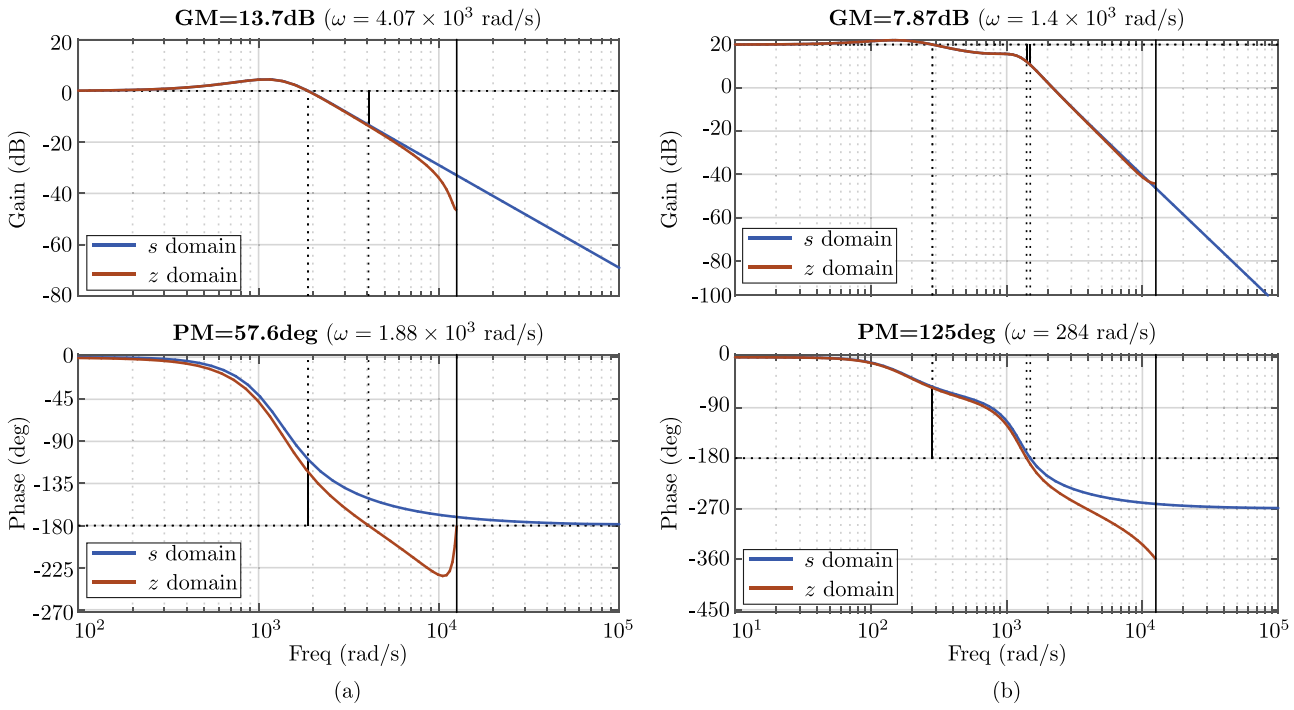

Fig. 10. The bode plot of (a) current controller in s and z domain (b) voltage controller in s and z domain.

insignificant at low-frequency range (i.e., one-fifth of the LCL filter resonant frequency). In this study, the current loop bandwidth is one-fifth of the LCL filter resonant frequency, and the voltage loop bandwidth is one-twentieth of the LCL filter resonant frequency. Therefore, it is reasonable to treat the LCL filter as a L filter well below the resonance frequency range.

4. Simulation results and discussion

The electrolyzer and converters are modeled using MATLAB®/Simulink® and PLECS. The system schematic is presented in Fig. 6 and parameters are given in Table 4.

In the following context, two case studies (THD measurements and voltage disturbance) are carried out to test the controller robustness and evaluate the THD of the designed system. Since the grid impedance is varying from case to case, two typical values: SCR=10 refers to a weak grid and SCR = 33 refers to a stiff grid, are considered in the following study. The designed electrolyzer system is connected to a medium voltage grid that belongs to the distribution network. Therefore, the X/R is chosen as 10 for a distribution system with overhead lines.

Table 4
Simulation parameters for a 500 kW alkaline electrolyzer system.

Symbol	Item	Value
Grid side parameter:		
P_{rate}	System rated power	500 kW
e_{abc}	Grid side voltage (line to line)	10 kV
f_{line}	Line frequency	50 Hz
SCR	Short circuit ratio	10 ∼ 33
X/R	Inductance to resistance ratio	10
$N_p : N_s$	Transformer turns ratio (Δ/Y)	4:1
Converter side parameter:		
$f_{sw.AFE}$	AFE switching frequency	4 kHz
$f_{sw.DC}$	PSFB switching frequency	2.5 kHz
L_g	Grid side inductance	31.9 mH
L_c	Converter side inductance	17.5 mH
C_f	Filter capacitance	0.6 μF
V_{dc}	DC link voltage	6 kV
Load side parameter:		
V_{load}	Rated load voltage	176 ∼ 262 V
I_{load}	Load current	0 ∼ 1900 A

4.1. Harmonic emission compatibility

The real electric grid contains a certain level of background harmonics. In order to emulate the real electrical grid condition, three different background harmonics (no harmonics, half-magnitude EN 50160 harmonics, and full-magnitude EN 50160 harmonics) are injected into the system [37]. The three-phase voltage and current at the point of connection (PoC) are obtained from the simulation with 2 μs step size. The harmonic analysis is conducted on phase-A current and voltage with 20ms time length. The obtained harmonic frequency spectrum is analyzed up to 9 kHz. The high order harmonics are attenuated with the LCL filter. Therefore, their magnitudes are not significant and neglected in the following analysis.

At the moment when this study is prepared, there is no dedicated regulations for large-scale grid-connected electrolyzer plant. As electrolyzer plants can convert electrical energy into chemical energy, they are treated as the electrical energy storage plant in this study. Therefore, the harmonic requirements in the Danish grid code for large-scale battery and electrical energy storage plants [34,35] are used as the standards for electrolyzer plants. In Figs. 11 and 12, the Std1 is the regulation for electrical energy storage facilities and Std2 is the regulation for battery plants.

4.1.1. SCR = 10

When the short circuit ratio is ten, it represents a weak distribution grid according to the Danish grid code. The THD is increasing along with the injected harmonic magnitude as shown in Fig. 11(a)–(c). There are two sidebands at which harmonic levels are higher than the average. The first sideband has a center frequency of 350 Hz which is around the bandwidth of the current control loop and the second sideband has a center frequency of 4 kHz which is the switching frequency of the AFE rectifier. The seventh harmonic has the highest magnitude in all different harmonic injection scenarios. When the full magnitude background harmonic is present, the seventh and thirteenth harmonics have a magnitude of 3.16% and 0.96%. Compared with the harmonic

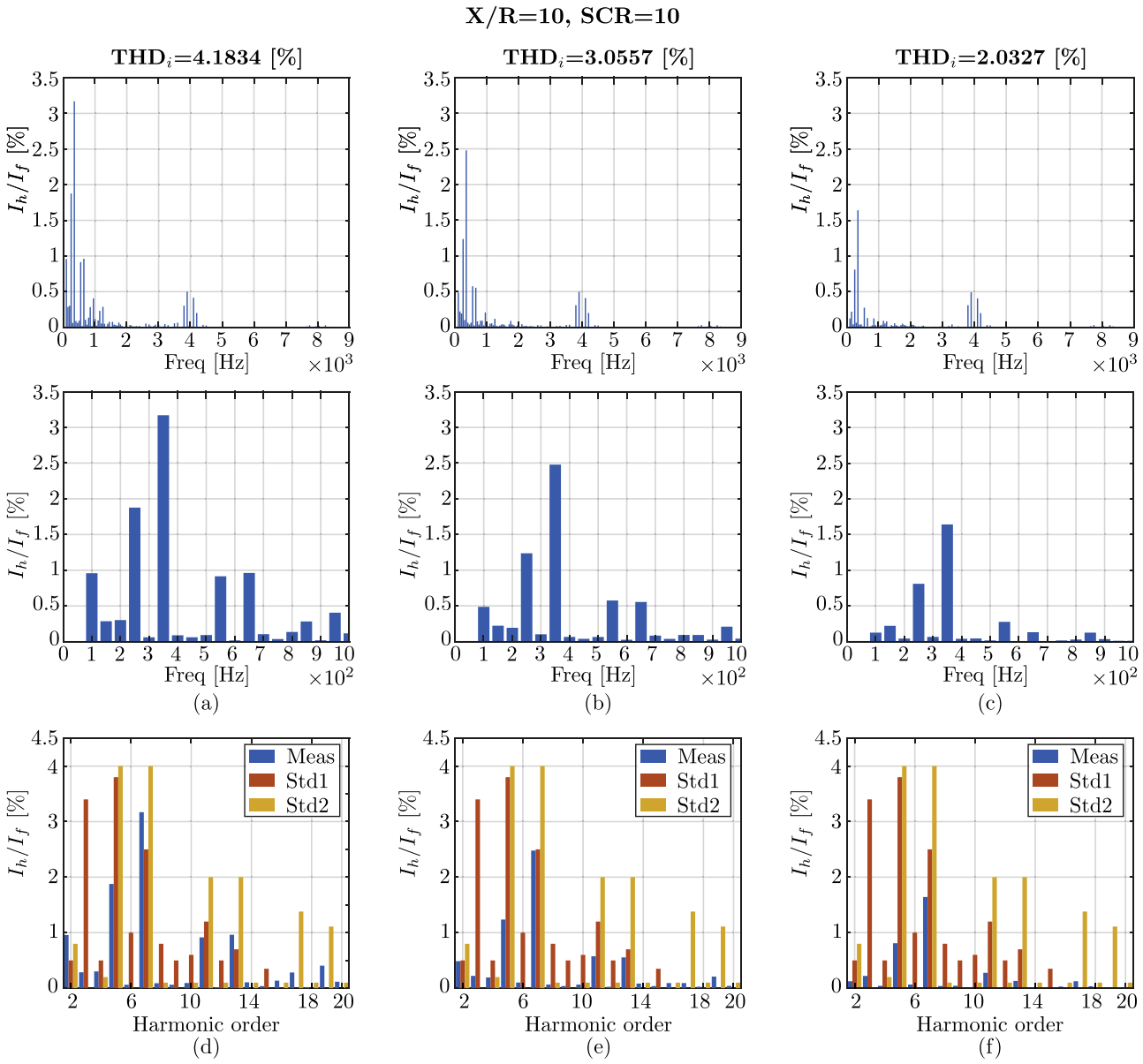

Fig. 11. The THD of the current at the PoC when $SCR = 10$, $X/R = 10$, and with (a) full magnitude EN-50160 harmonic injection, (b) half magnitude EN-50160 harmonic injection, or (c) no harmonic injection. The corresponding current harmonics compared with THD standard [34,35] for the case (d) full magnitude EN-50160 harmonic injection, (e) half magnitude EN-50160 harmonic injection, (f) no harmonic injection.

limitation for electrical energy storage plants, it exceeds the limited value by 0.66% for the seventh harmonic, and 0.26% for the thirteen harmonic. When the half-magnitude background harmonic is present, the magnitude of the seventh and thirteen harmonics are 2.47% and 0.55%. They are within the harmonic limitation for electrical energy storage plants and battery plants. When no background harmonic is present, the magnitude of the seventh and thirteen harmonics are 1.6% and 0.13%. All the harmonic components are within the harmonic limitation for electrical energy storage plants and battery plants in the Danish grid code.

4.1.2. $SCR = 33$

When the short circuit ratio is thirty-three, it represents a stiff distribution grid according to the Danish grid code. The THD is increasing along with the injected harmonic magnitude as shown in Fig. 12(a)–(c). There are two sidebands at which harmonic levels are higher than the average. The first sideband has a center frequency of 350 Hz which is around the bandwidth of the current control loop and the second sideband has a center frequency of 4 kHz which is the switching frequency of the AFE rectifier. The seventh harmonic has the highest magnitude in all different grid scenarios. When the full magnitude background harmonic is present, the seventh and thirteenth harmonics have a magnitude of 3.27% and 0.98%. Compared with the harmonic limitation for electrical energy storage plants, it exceeds the limited value by 0.77% for the seventh harmonic, and 0.28% for the thirteen harmonic. Compared with the weak grid case, the seventh and thirteenth harmonics are increased by 0.11% and 0.02%. When the half-magnitude background harmonic is present, the magnitude of the seventh and thirteen harmonics are 2.5% and 0.57%. They are within the harmonic limitation for electrical energy storage plants and battery plants. When no background harmonic is present, the magnitude of the seventh and thirteen harmonics are 1.66% and 0.13%. All the harmonic components are within the harmonic limitation for electrical energy storage plants and battery plants in the Danish grid code. Because the lower short circuit ratio results in a larger grid impedance value, the harmonics injected from the grid are attenuated with the grid

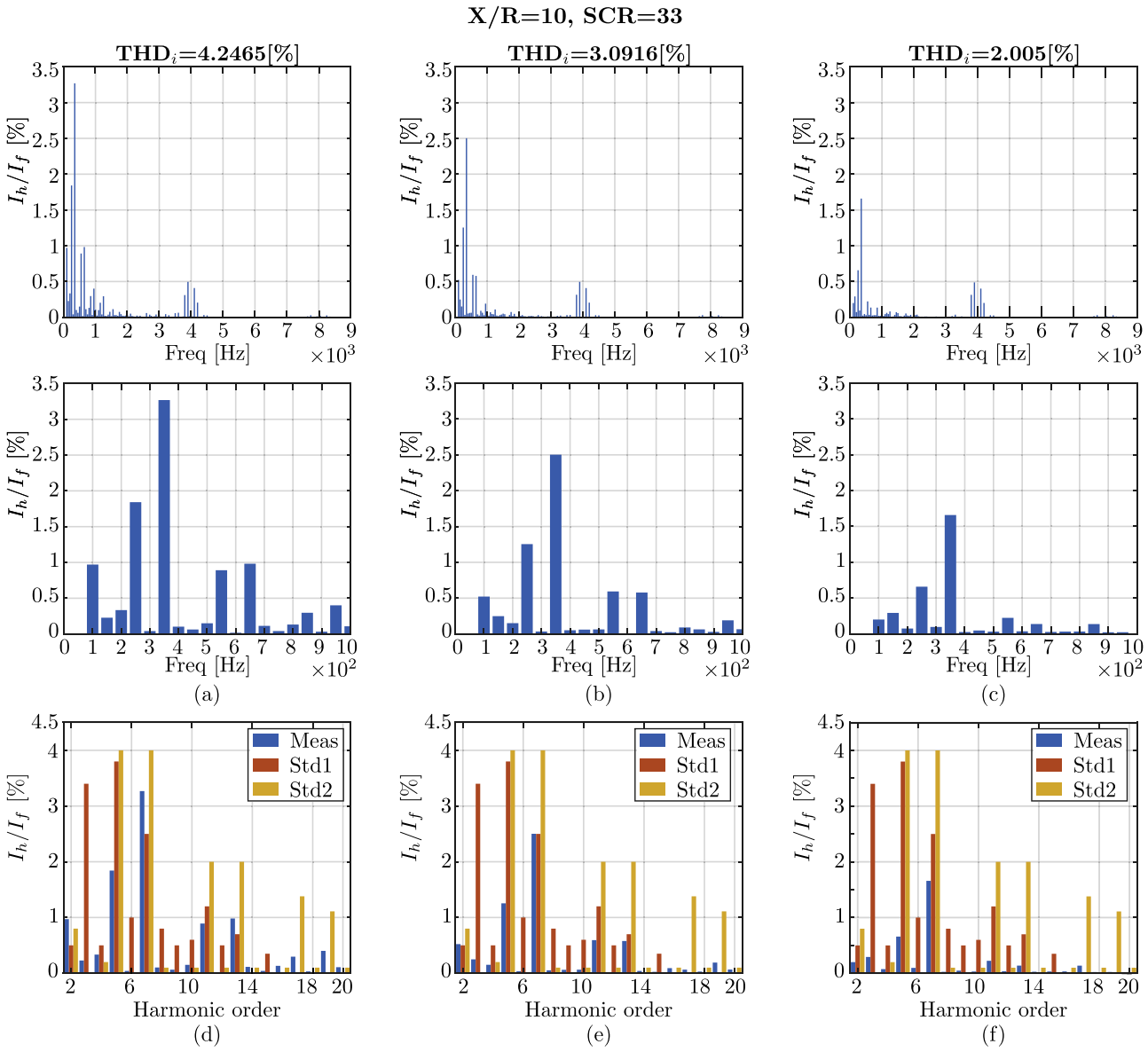

Fig. 12. The THD of the current at the PoC when $SCR = 33$, $X/R = 10$, and with (a) full magnitude EN-50160 harmonic injection, (b) half magnitude EN-50160 harmonic injection, or (c) no harmonic injection. The corresponding current harmonics compared with THD standard [34,35] for the case (d) full magnitude EN-50160 harmonic injection, (e) half magnitude EN-50160 harmonic injection, (f) no harmonic injection.

impedance. Therefore, the total harmonic distortion is lower for a lower short-circuit-ratio case. For no harmonic injection case, the THD between the strong grid and weak grid has a negligible difference (0.027%). Since the control loop bandwidth and switching frequency are the same in both cases, the resulting harmonic sidebands are the same as well [38].

The grid harmonics would propagate to the electrolyzer stacks if the LCL filter is not properly designed. These harmonics would appear in the current ripple in the current supply to the electrolyzer stacks. The current ripple leads to voltage variation across the terminal of the electrolyzer, which results in power consumption variation. The varied power consumption indicates the hydrogen and oxygen production rate variation. In Fig. 13, the hydrogen and oxygen production rates are presented with different filter values. In the case of a 3 mH filter inductor, the harmonics from the grid are properly attenuated. Therefore, the current ripple in the electrolyzer current is negligibly small, and the hydrogen and oxygen production rates have a lower variation. In comparison, the 0.3 mH filter results in a higher current ripple in the electrolyzer supply current. Therefore, the hydrogen and oxygen

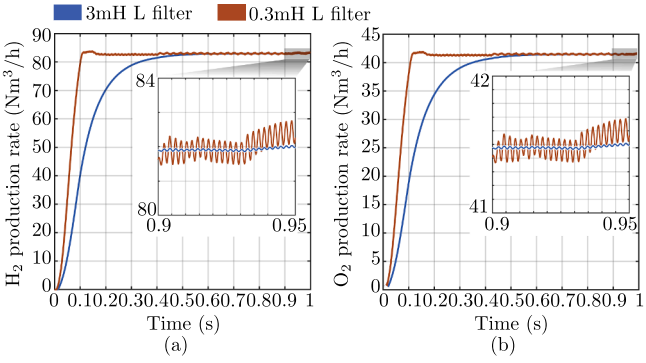

Fig. 13. The harmonics impacts on the hydrogen and oxygen production rate.

production rates are affected by the current ripples. The line frequency and ninth-order harmonics are present in the current ripple, hydrogen, and oxygen production rate. When the 3 mH filter is used, the electrolyzer supply current has a lower ramp-up speed compared with the case of 0.3 mH filter. Therefore, the corresponding hydrogen and oxygen production rate for 3 mH filter take a longer time to reach the rated condition.

4.2. Voltage deviation

According to the Danish grid code, energy storage facilities must be able to withstand voltage deviations in the PoC under normal and abnormal operating conditions. The normal operating voltage has a maximum 10% voltage deviation at the PoC and the abnormal operating voltage can have a maximum 85% voltage dip. However, ±20% voltage deviation is more common in real applications. In the following part, −10% and −20% voltage deviation at the grid side are conducted to test the response of the designed system and controller robustness.

In Fig. 14, 10% and 20% voltage dips occur at the grid side. For 10% grid voltage dip, the DC link voltage decreases 132 V when SCR = 33 (small grid impedance), and 149 V when SCR = 10 (large grid impedance). For 20% grid voltage dip, the DC link voltage decreases 288 V when SCR = 33 (stiff grid conditions), and 299 V when SCR = 10 (weak grid conditions). Since the grid impedance is smaller when SCR = 33 compared with SCR = 10, a lower voltage drop across the grid impedance and higher DC link voltage can be obtained. For SPWM modulation adopted in this study, the required AC voltage should have a phase peak value of 3 kV to maintain the 6 kV DC link voltage. However, the 20% voltage dip makes the grid side voltage below 3 kV, which results in a large DC link voltage drop. One possible solution is to use a more efficient modulation strategy, for example, discontinuous PWM or third harmonic injection [39,40].

In Fig. 15, the *dq*-axis current error signals are compared at 10% and 20% grid voltage dips. Before the voltage dips occur in the grid, the system is operating in a steady state where the *d*-axis current reference has a small value and the *q*-axis current reference is zero. Since a certain amount of power is required to charge the electrolyzer, the measured *d*-axis current is larger than the reference signal which results in a negative error signal. When voltage dips occur, the *d*-axis current reference increases, which reduces the magnitude of the error signals. Since 20% voltage deviation results in a larger *d*-axis current reference signal than 10% voltage deviation, the magnitude of *d*-axis current error signal is larger than the 10% voltage deviation case as well.

The *q*-axis current error signal is due to the reactive components (i.e., LCL filters and DC link capacitors) requiring a certain amount of reactive power. Since the voltage dip that occurred in the system affects the amount of reactive power absorbed by these reactive components, hence the magnitude of *q*-axis current error signal is changing with the magnitude of voltage dips.

5. Conclusion

In this work, we present a converter-level modeling study for a 500 kW alkaline electrolyzer power supply. The alkaline electrolyzer is modeled with electrochemical equations and characterized based on the technical data of an alkaline electrolyzer cell. The characterized electrolyzer mode presents a relative error below 0.3%. With the characterized electrolyzer model, the active front end and phase shifted full bridge converter topology is selected as the power supply to the electrolyzer stack. The corresponding controller and filter design guidelines are concluded considering on the non-linearity of the electrolyzer load. With MATLAB®/Simulink® and PLECS, the 500 kW alkaline electrolyzer power supply system is tested at different grid conditions. From the simulation result, the designed system comply with the harmonic requirements in the Danish grid code for electrical energy storage and battery plants.

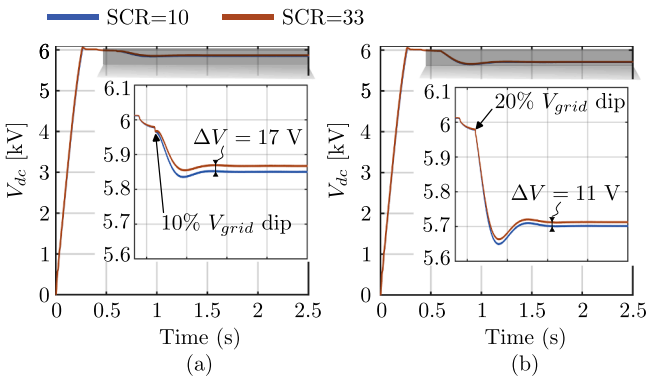

Fig. 14. AFE rectifier DC link voltage subject to (a) 10% grid voltage dip, (b) 20% grid voltage dip.

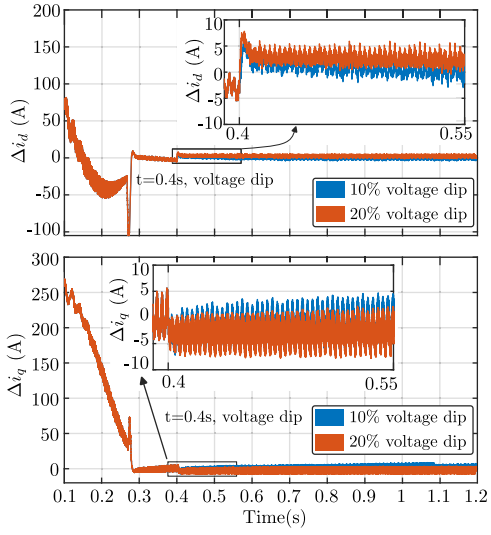

Fig. 15. Current controller error when SCR = 10.

Declaration of Competing Interest

The authors declare that they have no known competing financial interests or personal relationships that could have appeared to influence the work reported in this paper.

Data availability

No data was used for the research described in the article.

Acknowledgement

Authors would like to acknowledge the financial support from EU-REACT Southern Jutland Lighthouse projects “Center for Green Energy and Sector Coupling” and “PtXConverter” respectively.

References

[1] I. R. E. Agency, What are the latest trends in renewable energies, 2022Accessed 08 October 2022, ([Online]).
[2] Energinet, Energy island in Denmark, 2022Accessed 08 October 2022, ([Online]).
[3] I.E. Agency, More of a good thing – is surplus renewable electricity an opportunity for early decarbonisation?, 2022Accessed 23 November 2022, ([Online]).
[4] D.E. Agency, The Government’s Strategy for Power-to-X, ([Online]).
[5] Sunfire, Sunfire-Hylink Soec-Technical Data, 2022Accessed 14 October 2022, ([Online]).
[6] D. APS, Electrolysis system with controlled thermal profile, 2022Accessed 23 November 2022, ([Online]).

[7] I.R.E. Agency, Hydrogen from Renewable Power, Technology Outlook for the Energy Transition, 2022Accessed 09 October 2022, ([Online]).
[8] G.H. System, HyProvide-A-series-brochure, 2022Accessed 12 October 2022, ([Online]).
[9] I.R.E. Agency, Hydrogen from renewable power, technology outlook for the energy transition, 2022Accessed 09 October 2022, ([Online]).
[10] ABB, DC power supply for electrolyzers, 2022Accessed 12 October 2022, ([Online]).
[11] PowerKraft, Rectifier For Electrolytic process, 2022Accessed 13 October 2022, ([Online]).
[12] A.P. Solution, THYROBOX DC 3, 2022Accessed 13 October 2022, ([Online]).
[13] D. Guilbert, S.M. Collura, A. Scipioni, DC/DC converter topologies for electrolyzers: state-of-the-art and remaining key issues, Int. J. Hydrogen Energy 42 (38) (2017) 23966–23985, https://doi.org/10.1016/j.ijhydene.2017.07.174.
[14] B. Yodwong, D. Guilbert, M. Phattanasak, W. Kaewmanee, M. Hinaje, G. Vitale, AC-DC converters for electrolyzer applications: state of the art and future challenges, Electronics 9 (6) (2020), 912.
[15] M. Chen, S.-F. Chou, F. Blaabjerg, P. Davari, Overview of power electronic converter topologies enabling large-scale hydrogen production via water electrolysis, Appl. Sci. 12 (4) (2022), https://doi.org/10.3390/app12041906.
[16] S.M. Collura, D. Guilbert, G. Vitale, M. Luna, F. Alonge, F. D'Ippolito, A. Scipioni, Design and experimental validation of a high voltage ratio DC/DC converter for proton exchange membrane electrolyzer applications, Int. J. Hydrogen Energy 44 (14) (2019) 7059–7072, https://doi.org/10.1016/j.ijhydene.2019.01.210.
[17] D. Guilbert, D. Sorbera, G. Vitale, A stacked interleaved DC-DC buck converter for proton exchange membrane electrolyzer applications: design and experimental validation, Int. J. Hydrogen Energy 45 (1) (2020) 64–79, https://doi.org/10.1016/j.ijhydene.2019.10.238.
[18] D. Concha, H. Renaudineau, M.S. Hernández, A.M. Llor, S. Kouro, Evaluation of DCX converters for off-grid photovoltaic-based green hydrogen production, Int. J. Hydrogen Energy 46 (38) (2021) 19861–19870, https://doi.org/10.1016/j.ijhydene.2021.03.129.International Journal of Hydrogen Energy Special Issue devoted to the 32nd International Conference ECOS 2019
[19] L. Török, L. Mathe, C.K. Nielsen, S. Munk-Nielsen, Modelling and control of three-phase grid-connected power supply with small dc-link capacitor for electrolysers. 2016 IEEE 16th International Conference on Environment and Electrical Engineering (EEEIC), 2016, pp. 1–6, https://doi.org/10.1109/EEEIC.2016.7555674.
[20] H. Zhang, Y. Lu, J. Zhang, A. Benigni, Real-time simulation of an electrolyzer with a diode rectifier and a three-phase interleaved buck converter. 2022 IEEE 13th International Symposium on Power Electronics for Distributed Generation Systems (PEDG), 2022, pp. 1–6, https://doi.org/10.1109/PEDG54999.2022.9923192.
[21] A. Iribarren, E.L. Barrios, H. Ibaiondo, A. Sanchez-Ruiz, J. Arza, P. Sanchis, A. Ursúa, Modelling and operation of 6-pulse thyristor rectifiers for supplying high power electrolyzers. 2022 IEEE 23rd Workshop on Control and Modeling for Power Electronics (COMPEL), 2022, pp. 1–8, https://doi.org/10.1109/COMPEL53829.2022.9829992.
[22] A. Ursúa, L. Marroyo, E. Gubía, L.M. Gandía, P.M. Diéguez, P. Sanchis, Influence of the power supply on the energy efficiency of an alkaline water electrolyser, Int. J. Hydrogen Energy 34 (8) (2009) 3221–3233, https://doi.org/10.1016/j.ijhydene.2009.02.017.
[23] O. Atlam, M. Kolhe, Equivalent electrical model for a proton exchange membrane (PEM) electrolyser, Energy Convers. Manag. 52 (8) (2011) 2952–2957, https://doi.org/10.1016/j.enconman.2011.04.007.
[24] R. Takahashi, H. Kinoshita, T. Murata, J. Tamura, M. Sugimasa, A. Komura, M. Futami, M. Ichinose, K. Ide, Output power smoothing and hydrogen production by using variable speed wind generators, IEEE Trans. Ind. Electron. 57 (2) (2010) 485–493, https://doi.org/10.1109/TIE.2009.2032437.
[25] A. Ursúa, P. Sanchis, Static–dynamic modelling of the electrical behaviour of a commercial advanced alkaline water electrolyser, Int. J. Hydrogen Energy 37 (24) (2012) 18598–18614, https://doi.org/10.1016/j.ijhydene.2012.09.125.2011 International Workshop on Molten Carbonates and Related Topics
[26] Ø. Ulleberg, Modeling of advanced alkaline electrolyzers: a system simulation approach, Int. J. Hydrogen Energy 28 (1) (2003) 21–33, https://doi.org/10.1016/S0360-3199(02)00033-2.
[27] M. Hammoudi, C. Henao, K. Agbossou, Y. Dubé, M. Doumbia, New multi-physics approach for modelling and design of alkaline electrolyzers, Int. J. Hydrogen Energy 37 (19) (2012) 13895–13913, https://doi.org/10.1016/j.ijhydene.2012.07.015.HYFUSEN
[28] M. Carmo, D.L. Fritz, J. Mergel, D. Stolten, A comprehensive review on PEM water electrolysis, Int. J. Hydrogen Energy 38 (12) (2013) 4901–4934, https://doi.org/10.1016/j.ijhydene.2013.01.151.
[29] Ø. Ulleberg, Simulation of autonomous PV-H2 systems: analysis of the phoebus plant design, operation and energy management. ISES 1997 Solar World Congress, Taejon, 1997.
[30] GreenHydrogen.dk, Siemens, DTU, and AU, HyProvide Large-Scale Alkaline Electrolyser (MW), 2022Accessed 21 October 2022, ([Online]).
[31] M. Liserre, F. Blaabjerg, S. Hansen, Design and control of an LCL-filter-based three-phase active rectifier, IEEE Trans. Ind. Appl. 41 (5) (2005) 1281–1291, https://doi.org/10.1109/TIA.2005.853373.
[32] I. Landau, A. Voda, The "symmetrische optimum" and the auto-calibration of PID controllers, IFAC Proc. Vol. 25 (14) (1992) 407–412, https://doi.org/10.1016/S1474-6670(17)50768-5.4th IFAC Symposium on Adaptive Systems in Control and Signal Processing 1992, Grenoble, France, 1-3 July
[33] R. Teodorescu, M. Liserre, P. Rodriguez, Grid Converter Control for WTS, John Wiley & Sons, Ltd, 2011, pp. 205–236, https://doi.org/10.1002/9780470667057.ch9.
[34] Energinet, Technical Regulation 3.3.1 for Electrical Energy Storage Facilities, 2022Accessed 18 October 2022a, ([Online]a).
[35] Energinet, Technical Regulation 3.3.1 for Battery Plants, 2022Accessed 18 October 2022 b, ([Online]b).
[36] Y. Tang, P.C. Loh, P. Wang, F.H. Choo, F. Gao, Exploring inherent damping characteristic of LCL-filters for three-phase grid-connected voltage source inverters. 2010 IEEE Energy Conversion Congress and Exposition, 2010, pp. 312–319, https://doi.org/10.1109/ECCE.2010.5618021.
[37] European Committee for Electrotechnical Standardization, Voltage characteristics of electricity supplied by public electricity networks, 2010.
[38] X. Wang, F. Blaabjerg, Harmonic stability in power electronic-based power systems: concept, modeling, and analysis, IEEE Trans. Smart Grid 10 (3) (2019) 2858–2870, https://doi.org/10.1109/TSG.2018.2812712.
[39] A. Hava, R. Kerkman, T. Lipo, A high-performance generalized discontinuous PWMalgorithm, IEEE Trans. Ind. Appl. 34 (5) (1998) 1059–1071, https://doi.org/10.1109/28.720446.
[40] A. Hava, R. Kerkman, T. Lipo, Simple analytical and graphical methods for carrier-based PWM-VSI drives, IEEE Trans. Power Electron. 14 (1) (1999) 49–61, https://doi.org/10.1109/63.737592.

Weihao Zhao received the M.Sc. degree in energy engineering with specializing in power electronics and drives from Aalborg University, Aalborg, Denmark, in 2022.

Morten Rahr Nielsen received the M.Sc. degree in energy engineering, with a specialization in power electronics and drives, from Aalborg University, Aalborg, Denmark, in 2022. He is currently a Research Assistant within the Department of Energy, Aalborg University. His current research interests include wide bandgap semiconductor devices and control of medium voltage power converters.

Martin Vang Kjær received the B.Sc. and M.Sc. degrees in energy technology with specializing in electrical energy engineering and power electronics and drives from Aalborg University, Aalborg, Denmark, in 2017 and 2020, respectively, where he is currently working toward the Ph.D. degree in applied power electronics with the Department of Energy. His research interests include intelligent power processing, reliable operation of distributed generation systems, and prognostics and health management of power converters.

Dr. Florin Iov (IEEE SM '06) received the M.Sc. degree in Electrical Engineering from "Transilvania" University of Brasov, Romania, in 1993 and a Ph.D. degree from "Lower Danube" University of Galati, Romania in 2003 with a special focus in the modeling, simulation and control of large wind turbines. He was staff member at Galati University, Romania from 1993 to 2001. Dr. Iov was with Institute of Energy Technology, Aalborg University, Denmark between 2001 and 2009 where he was mainly involved in research projects regarding grid integration of wind power. From 2010 to 2012 he held a position as Power System Research Specialist in Vestas Wind Systems working with new ancillary services for augmented wind power plants. Since 2013 Dr. Iov is with Institute of Energy Technology, Aalborg University, focusing on research and teaching on smart grids, intelligent energy systems and cross-sector coupling. His research areas cover: Modelling, simulation and control of renewable/hybrid energy systems; Power electronic converters for grid integration of renewable/hybrid energy systems; Ancillary services; Grid code compliance and market participation of hybrid power plants; Stability of power systems with high penetration of renewable generation plants; Monitoring, operation, control and protection of smart distribution systems; Power-to-X and carbon capture technologies and their integration; Model based Design using cyber-physical systems (Real-Time Digital Twins). He is author/co-author of 170+ papers published in international journals and conference proceedings and 50+ research reports available on the public domain. He is inventor in two patents of wind power plant control.

Stig Munk-Nielsen (Member, IEEE) received the M.Sc. and Ph. D. degrees from Aalborg University, Aalborg, Denmark, in 1991 and 1997, respectively, both in three-phase resonant dc-link converters.,He is currently a Professor with the Department of Energy, Aalborg University. In the last ten years, he was involved in 10 research projects. He has authored and coauthored 244 international power electronics papers and applied for 4 patents. His research interests include LV and MV Si, SiC, and GaN technology, including power converter circuits and components.